Maximum Likelihood Segmentation of Ultrasound Images with Rayleigh Distribution

Alessandro Sarti, Cristiana Corsi, Elena Mazzini, and Claudio Lamberti

***Abstract*—This study presents a geometric model and a computational algorithm for segmentation of ultrasound images. A partial differential equation (PDE)-based flow is designed in order to achieve a maximum likelihood segmentation of the target in the scene. The flow is derived as the steepest descent of an energy functional taking into account the density probability distribution of the gray levels of the image as well as smoothness constraints. To model gray level behavior of ultrasound images, the classic Rayleigh probability distribution is considered. The steady state of the flow presents a maximum likelihood segmentation of the target. A finite difference approximation of the flow is derived, and numerical experiments are provided. Results are presented on ultrasound medical images as fetal echography and echocardiography.**

I. Introduction

In the medical imaging research area, clinical parameters quantification is a challenging goal because it represents a strong clinical need due to the important diagnostic and therapeutic implications in the management of patients. Examples include parameters such as left ventricular cavity volumes, cardiac output, ejection fraction, and mass that are important indices for serial assessments of myocardial function. For the extraction of these parameters, the most difficult step to accomplish in a fast, accurate, and proper way is represented by image segmentation. In clinical practice the quantification of these indices is generally performed by manual tracing, which is a time-consuming and subjective procedure, and by the application of geometrical assumptions that could introduce measurement errors in presence of pathologies. Therefore, a rapid, accurate, reproducible, and noninvasive method of calculating these indices would be important.

Medical data can be acquired with a variety of imaging modalities; in this study we refer to echography whose primary advantage over other imaging modalities is the ability to generate real-time images of anatomy without the use of ionizing radiation. Moreover, echography is a widely available, noninvasive, and low-cost clinical modality for imaging. However, ultrasound images are difficult candidates for shape recovery because of low signal/noise ratio which greatly reduces the observable details within such images; main degradation mechanisms are due to Rayleigh and scattering diffraction of acoustical waves, little contrast between soft tissue and blood, nonhomogeneous acoustical characteristics of muscles. Accordingly, precision and accuracy of the derived measurements often are compromised.

Several approaches have been reported in the literature for automated or semiautomated border detection from ultrasound data, based on different methods: statistical Markov random fields [1]–[5], multidimensional space-frequency methods [6], [7], fuzzy logic [8]–[10], neural networks [11], [12], active contours models (snakes) [13]. The classical active contour models are based on the evolution of a curve attracted by image boundaries in order to detect objects. Malladi *et al.* [14] implemented segmentation methods with robust numerical techniques based on level-set models. Level-set methods, introduced first by Osher and Sethian [15], have been extensively used to track the evolution of fronts in a variety of applications, including segmentation of echographic images [16]–[22].

These methods embed the desired interface as the zero level set of an implicit function, then use finite differences to approximate the solution of the partial differential equation. The aforementioned approaches for segmentation are edge-based (i.e., they evolve a curve with a speed function, depending on a precomputed edge indicator). It is very effective in case edges are true discontinuities in the image, and the signal-to-noise ratio is not too low. Lately a region-based level-set based method has been proposed by Chan and Vese [23] to segment images with smooth or vanishing boundaries. In this approach, the speed of curve evolution involves integral quantities (like mean values of the gray-level image pixels inside and outside the curve) instead of differential quantities (like image gradient). This approach is very effective in case of smooth edges or low signal/noise ratio.

In the following we will briefly review the two approaches.

The Malladi-Sethian edge-based method is able to perform segmentation irrespective to shape topology. The algorithm is built in two steps. First an edge indicator function:

$$g(x,y) = \frac{1}{1 + (|\nabla G_\sigma(x,y) \star I(x,y)|)^2}$$

is used to detect local edges, where $|G_\sigma \star I|$ is a smoothed version of the given image $I : \Omega \subset R^2 \rightarrow R$ with a Gaussian kernel:

$$G_\sigma(x,y) = \frac{\exp(-(\sqrt{x^2+y^2})/\sigma^2)}{\sigma\sqrt{\pi}}.$$

Manuscript received November 10, 2003; accepted December 17, 2004.

The authors are with the Department of Electronics, Computer Science and Systems, University of Bologna, Bologna, I-40136, Italy (email: asarti, ccorsi, clamberti@deis.unibo.it).

During the second stage, a curve evolution inside the object is implemented, in which the curve speed is tuned by the edge indicator to stop the evolving curve on the boundaries of the desired object. If the curve C is represented by the zero level set of an implicit function $\phi : \Omega \to R$ such that $C = \{(x, y) \in \Omega : \phi(x, y) = 0\}$, the evolution equation is:

$$\begin{cases} \partial_t \phi = |\nabla\phi| g(|\nabla I|) div\dfrac{\nabla\phi}{|\nabla\phi|} + \nu\nabla g(|\nabla I|)\cdot\nabla\phi & \\ & \text{in } \Omega\times]0,\infty[\\ \phi(x,y,0) = \phi_0(x,y) & \text{in } \Omega \\ \phi(x,y,t) = \min(\phi_0(x,y)) & \text{on } \partial\Omega \end{cases}, \quad (1)$$

where ϕ is the level-set function. The first term on the right side moves the curve in the normal direction with a speed equal to the Euclidean curvature of level curves $div(\nabla\phi/|\nabla\phi|)$ weighted by the edge indicator $g(|\nabla I|)$. The second term corresponds to a pure passive advection of the curve along the underlying velocity field $-\nabla g$, that is a vector field pointing always toward the existing boundaries. The constant ν is added to increase the evolution speed in order to attract the curve toward the boundary. The equation has been approximated with finite differences [15].

Chan and Vese [23] proposed a different model, based on a region-based approach: the model is well adapted to situations in which images are noisy, and it is difficult to extract the boundary of the desired object. Their method considers the evolution of a curve C in order to minimize the energy functional:

$$F(C, c_1, c_2) = \mu\cdot(length(C)) + \nu\cdot area(inside(C)) + \lambda_1\int_{inside(C)} |I(x,y)-c_1|^2 + \lambda_2\int_{outside(C)} |I(x,y)-c_2|^2,$$

where c_1 and c_2 are the averages of I, respectively, inside and outside C, and $\mu \geq 0$, $\nu \geq 0$, λ_1, λ_2 are fixed parameters.

The associated level set flow is computed by considering again $C = \{(x, y) \in \Omega : \phi(x, y) = 0\}$ and keeping c_1 and c_2 fixed as:

$$\begin{cases} \partial_t\phi = \delta(\phi)\left[\mu div\left(\dfrac{\nabla\phi}{|\nabla\phi|}\right) - \nu - \lambda_1(I-c_1)^2 + \lambda_2(I-c_2)^2\right] & \\ & \text{in } \Omega\times]0,\infty[\\ \phi(0,x,y) = \phi_0(x,y) & \text{in } \Omega \\ \dfrac{\delta(\phi)}{|\nabla\phi|}\dfrac{\partial\phi}{\partial n} = 0 & \text{on } \partial\Omega \end{cases}, \quad (2)$$

where $\delta()$ is the Dirac function and n denotes the exterior normal to the boundary $\partial\Omega$.

In this paper we take a different view of the segmentation problem by keeping the region-based approach of Chan-Vese and embedding in the segmentation model the a priori knowledge of statistical distribution of grey levels in ultrasound data [24], [25]. In particular concerning ultrasound images, we note that image pixels are modeled as Rayleigh distributed random variables. Then the proposed method drives the curve evolution to achieve a maximum likelihood segmentation of the target, with respect to the statistical distribution law of image pixels. We apply our method for segmentation of echography (Rayleigh distribution), even if the level set maximum likelihood method also can be applied in other areas of medical imaging as computed tomography and magnetic resonance imaging angiography, mammography (Poisson distribution), and photographic images of melanoma (Gaussian distribution).

The outline of the paper is as follows. In Section II we introduce the main energy functional and compute its first variation to obtain the associated Euler-Lagrange equation. A level set formulation for the associated flow is derived. In Section III we present a finite-difference approximation of the flow based on propagation of surfaces by curvature (PSC) numerical schemes introduced in [15]. In Section IV we show results regarding the verification of the Rayleigh distribution assumption, the validation we performed comparing our results with manual tracings, the application of the method to different kinds of ultrasound medical images. We end the paper with a brief concluding section.

II. Theory

A. The Main Functional

Let us consider an image I as a real positive function defined in a rectangular domain $\Omega \subset R^2$. The gray levels are assumed to be uncorrelated and independently distributed. Thus, they are characterized by their respective probability density function (pdf) $p(I)$.

Now we define a closed curve C partitioning the image domain in an "inside" Ω_i and an "outside" Ω_e and denote with $P_i = \prod_{\Omega_i(C)} p(I)$ the probability of the random field inside the curve and with $P_e = \prod_{\Omega_e(C)} p(I)$ the probability outside the curve. Without any a priori knowledge about the shape of the object to be detected, we look for the curve C that maximizes the likelihood function given by the product of the inner and the outer probability [26]:

$$P[I|C] = P_i\, P_e. \quad (3)$$

Because the log function is strictly increasing, the maximum value of $P[I|C]$, if it exists, will occur at the same points as the maximum value of $l(I, C) = \log(P[I|C])$. This latter function is the log likelihood, and in many cases it is easier to work with it than with the likelihood function. Indeed, the product structure of the probability function is transformed in a summation or integral structure of the log likelihood. Passing to the continuous limit, we replace the sum with the integral and obtain:

$$l(I,C) = \log P_i + \log P_e = \int_{\Omega_i(C)} \log p(I)\, dxdy + \int_{\Omega_e(C)} \log p(I)\, dxdy. \quad (4)$$

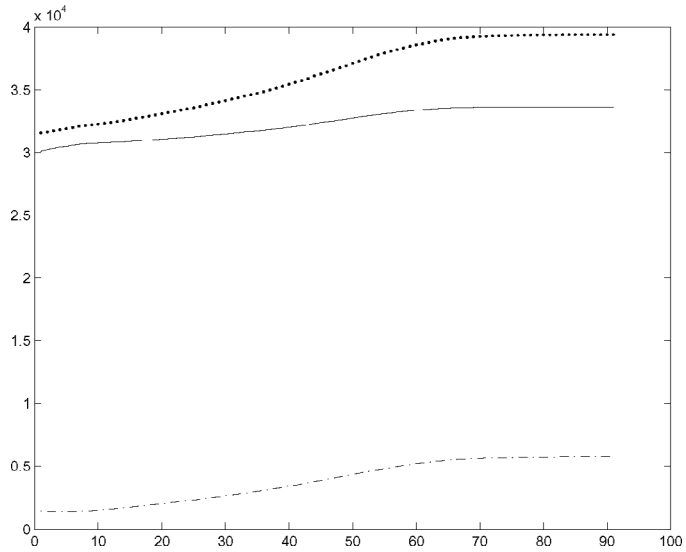

Fig. 1. Behavior of the terms $\log P_i$ (dashed line), $\log P_e$ (solid line) that appear in the expression of l, and of the log likelihood l (point line) during the evolution of the curve C.

To perform a maximum likelihood segmentation of the target, we need to maximize the functional l with respect to variation of the curve C. Because $p(I)_{rayleigh} = I(x,y)/\sigma^2 \exp\left(-I(x,y)^2/2\sigma^2\right)$, the corresponding log-likelihood is given by [25]:

$$\log P_i + \log P_e = A_i \log\left(\frac{1}{A_i}\int_{\Omega_i(C)} I(x,y)^2 dxdy\right) + A_e \log\left(\frac{1}{A_e}\int_{\Omega_e(C)} I(x,y)^2 dxdy\right), \quad (5)$$

where A_i, e, A_e are, respectively, the number of pixels in $\Omega_i(C)$ and $\Omega e(C)$ and the parameters of the pdf have been estimated in the Appendix [25]. The behavior of $\log P_i$, $\log P_e$, and l as the curve C is moving is visualized in Fig. 1. The functional l shows a plateau (maximum) when the curve has segmented the target, i.e., the curve introduces a partition of the image in two maximally homogeneous areas.

In order to obtain a well-posed and well-conditioned problem, we need to introduce a regularization in the shape of the curve. To address this, a length term has been introduced as in [23], to give:

$$F = \mu \cdot (length(C)) - A_i \log\left(\frac{1}{A_i}\int_{\Omega_i(C)} I(x,y)^2 dxdy\right) - A_e \log\left(\frac{1}{A_e}\int_{\Omega_e(C)} I(x,y)^2 dxdy\right). \quad (6)$$

An example of the time evolution of the initial condition considering the maximum likelihood algorithm applied to a synthetic image affected by Rayleigh noise is shown in Fig. 2.

B. The Associated Flow

To compute the first variation of (6), it is useful to introduce an auxiliary function $\phi : \Omega \to R$ such that $\phi(x,y) < 0$ in Ω_i and $\phi(x,y) > 0$ in Ω_e, defining implicitly the curve C as the zero level set of ϕ. Then the energy functional (6) can be rewritten using the Heaviside function $H(\phi)$, as:

$$F = \mu \int_\Omega |\nabla H(\phi)| dxdy - \left[A_i \log\left(\frac{1}{A_i}\int_\Omega I(x,y)^2 H(\phi) dxdy\right) + A_e \log\left(\frac{1}{A_e}\int_\Omega I(x,y)^2 (1-H(\phi)) dxdy\right)\right], \quad (7)$$

where:

$$A_i = \int_\Omega H(\phi) dxdy,$$
$$A_e = \int_\Omega (1 - H(\phi)) dxdy,$$

and [27]:

$$length\{\phi = 0\} = \int_\Omega |\nabla H(\phi)| dxdy = \int_\Omega \delta(\phi)|\nabla\phi| dxdy.$$

The associated Euler-Lagrange equations are derived in the Appendix and leads to:

$$0 = \delta(\phi)\left[\mu div\left(\frac{\nabla\phi}{|\nabla\phi|}\right) + \log\left(\frac{1}{A_i}\int_{\Omega_i} I^2 dxdy\right) + \frac{A_i I^2 - \int_{\Omega_i} I^2 dxdy}{\int_{\Omega_i} I^2 dxdy} - \log\left(\frac{1}{A_e}\int_{\Omega_e} I^2 dxdy\right) - \frac{A_e I^2 - \int_{\Omega_e} I^2 dxdy}{\int_{\Omega_e} I^2 dxdy}\right]. \quad (8)$$

The first term of the right-hand side denotes the Euclidean curvature of level curves. It represents the speed of curve evolution in the normal direction.

In level-set methods, the Euler-Lagrange equation for ϕ acts only locally, on a few level curves around $\phi = 0$. To extend the evolution to all level sets of ϕ, we replace $\delta(\phi)$ with $|\nabla\phi|$ [28]. Thus, (8) will act on all the level curves, of course stronger on the zero level curve. From (8), we simply get the associated flow as:

$$\begin{cases} \partial_t\phi = |\nabla\phi|\left[\mu div\left(\frac{\nabla\phi}{|\nabla\phi|}\right) + \log\left(\frac{1}{A_i}\int_{\Omega_i} I^2 dxdy\right) + \frac{A_i I^2 - \int_{\Omega_i} I^2 dxdy}{\int_{\Omega_i} I^2 dxdy} - \log\left(\frac{1}{A_e}\int_{\Omega_e} I^2 dxdy\right) - \frac{A_e I^2 - \int_{\Omega_e} I^2 dxdy}{\int_{\Omega_e} I^2 dxdy}\right] & \text{in } \Omega\times]0,\infty[\\ \phi(x,y,0) = \phi_0(x,y) & \text{in } \Omega \\ \frac{\delta(\phi)}{|\nabla\phi|}\frac{\partial\phi}{\partial n} = 0 & \text{on } \partial\Omega. \end{cases} \quad (9)$$

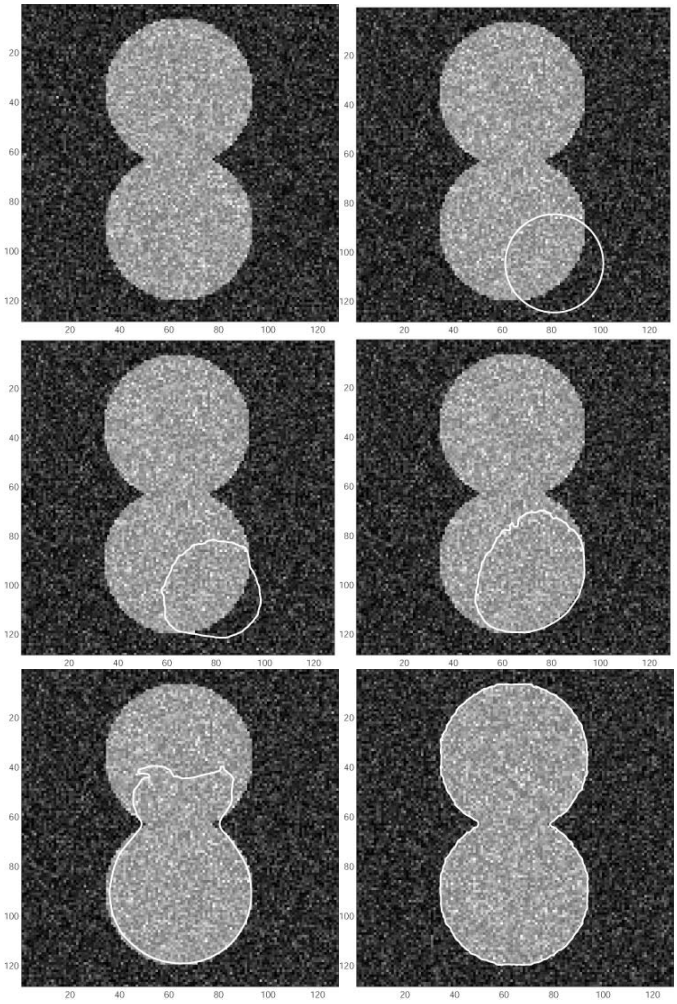

Fig. 2. Example of the time evolution of the initial condition (white circle in the upper right panel) considering the maximum likelihood algorithm applied to a synthetic image effected by Rayleigh noise (upper left panel). Images represents the solution of our model at different times, during which the curve moves to reach the final steady state.

where $\phi(x, y, 0)$ is an initial function with the property that its zero level set corresponds to the position of the initial front. Typically it is defined by:

$$\phi(x, y, 0) = \pm d, \tag{10}$$

where d is the signed distance function from each point to the initial front [29]. $(\delta(\phi)/|\nabla\phi|)(\partial\phi/\partial n) = 0$ are the boundary conditions. The evolution process will stop when the region probability terms of the inside regions do equal the terms of outside regions, up to regularization of boundaries. When working with level set and Dirac delta function, in order to prevent that the level set function becomes too flat or too steep, a standard procedure is to reinitialize ϕ to the signed distance function to its zero level curve as in [28] and [23]. This can be seen as a rescaling and regularization. Only for a few numerical results we have

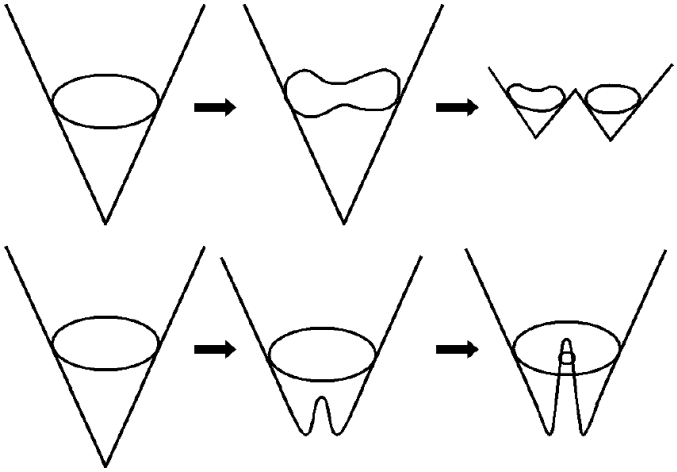

Fig. 3. Graphical explanation of the reinitialization process: it prevents any topological changes due to the arising of new regions that can be generated only by splitting of an existing contour (upper figures) and not by arising of new maxima in the level set function (bottom figures).

applied the re-initialization, solving the following evolution equation [30]:

$$\begin{cases} \psi_\tau = sign(\phi(t))(1 - |\nabla\psi|), \\ \psi(x, y, 0) = \phi(x, y, t) \end{cases}, \tag{11}$$

where $\phi(x, y, t)$ is the solution of (9) at time t. Then the new $\phi(x, y, t)$ will be ψ, such that ψ is obtained at the steady state of (11). The solution $\psi(x, y, t)$ will have the same zero level set of the $\phi(x, y, t)$, and everywhere $|\nabla\phi|$ will converge to 1. In this way, any topological changes due to the arising of new regions are prevented. In other words, new regions can be generated only by splitting of an existing contour and not by arising of new maxima in the level-set function as graphically explained in Fig. 3. To discretize this term, we use the scheme proposed in [28].

III. Numerical Approximation

In this section, we show how to approximate (9) with finite differences. For following fronts propagating with curvature-dependent speed, we exploit propagation of surface by curvature (PSC) algorithms introduced in [15]. These algorithms approximate the equations of motion, which resemble Hamilton-Jacobi equations with parabolic right-hand sides, by using techniques coming from hyperbolic conservation laws. In this way a correct entropy-satisfying approximation of the difference operator is built.

Let us consider a rectangular uniform grid in space-time (t, x, y); then the grid consists of the points $(t_n, x_l, y_m) = (n\Delta t, l\Delta x, m\Delta y)$. Following standard notation, we denote by ϕ^n_{lm} the value of the function ϕ at the grid point (t_n, x_l, y_m). The first term in (9) is a parabolic contribu-

tion to the equation of motion, and it is approximated with central differences as follows:

$$Kg = |\nabla\phi| div\left(\frac{\nabla\phi}{|\nabla\phi|}\right) = \frac{D_{lm}^{0x^2} D_{lm}^{0yy} - 2D_{lm}^{0x} D_{lm}^{0y} D_{lm}^{0xy} + D_{lm}^{0y^2} D_{lm}^{0xx}}{D_{lm}^{0x^2} + D_{lm}^{0y^2}}, \quad (12)$$

where D is a finite-difference operator on ϕ_{lm}^n and the superscript $\{0\}$ indicates central difference. The term $|\nabla\phi|$ can be approximated using the upwind schemes [15]:

$$G = \left\{ \begin{array}{l} \Big[\left(\max\left(D_{lm}^{-x}, 0\right)\right)^2 + \left(\min\left(D_{lm}^{+x}, 0\right)\right)^2 \\ + \left(\max\left(D_{lm}^{-y}, 0\right)\right)^2 + \left(\min\left(D_{lm}^{+y}, 0\right)\right)^2 \Big]^{1/2} \end{array} \right\}, \quad (13)$$

where the superscripts $\{-, +\}$ indicate backward and forward differences, respectively, and the superscripts $\{x, y\}$ indicate the direction of differentiation. This scheme is used to avoid the front passing through itself during the evolution when a corner develops.

We then can write the complete first order scheme to approximate (9) as follows:

$$\phi_{lm}^{n+1} = \phi_{lm}^n + \Delta t \left\{ \mu Kg\left(\phi_{lm}^n\right) + G\left(\phi_{lm}^n\right) \left[\begin{array}{l} \log\left(\dfrac{1}{A_i\left(\phi_{lm}^n\right)} \displaystyle\sum_{\Omega_i} I_{ij}^2\right) \\ + \dfrac{A_i\left(\phi^n\right) I_{lm}^2 - \sum_{\Omega_i} I_{ij}^2}{\sum_{\Omega_i} I_{ij}^2} \\ - \log\left(\dfrac{1}{A_e\left(\phi_{lm}^n\right)} \displaystyle\sum_{\Omega_e} I_{ij}^2\right) \\ - \dfrac{A_e\left(\phi^n\right) I_{lm}^2 - \sum_{\Omega_e} I_{ij}^2}{\sum_{\Omega_e} I_{ij}^2} \end{array} \right] \right\}. \quad (14)$$

The time step Δt is upper bounded by the Courant-Friedrich-Levy (CFL) condition that ensures the stability of the evolution [31]. For further details on the derivation of this condition, we refer to [15].

IV. Results

The method has been applied to a variety of ultrasound images of clinical interest. Table I summarizes the experimental details for all the data we used in the study. All of them have been acquired as digital output of the ultrasound equipment containing the envelope of the radio-frequency signal, and we did not have access to the radio-frequency signal directly. In a subset of images, only qualitative analysis has been performed and for most of acquired data a quantitative analysis has been applied. Quantitative analysis included: verification of the assumption of Rayleigh distribution and comparison of the results of our segmentation with the results derived from manual tracing.

To verify the assumption of Rayleigh distribution on all the images, we compared the theoretical Rayleigh distribution with the histogram of the experimental ultrasound images as suggested in [32], [33] and we performed the Kolmogorov Smirnov test following Georgiou and Cohen [34]. The estimation of the probability density function from the samples was performed applying the maximum likelihood algorithm and the root mean square error of the estimation was calculated for each fitting. In Fig. 4 we present an example of the Rayleigh probability density function and the measured speckle pattern histogram of our image. For this example the root mean square error (rmse) of the estimation resulted in 0.019. For the entire data set we processed, the mean rmse was 0.082. The Kolmogorov Smirnov test was performed on uniform regions of myocardium. The hypothesis of Rayleigh distribution was accepted on 13 of 15 images, by setting the test significance at a 5% level ($p < 0.05$). In the worst case in which the hypothesis was accepted, the observed Kolmogorov Smirnov statistic was 0.082 and the cutoff value for determining if this statistic was significant resulted in 0.09.

A. Qualitative Results

The simulations were performed in Matlab 6.1 (The MathWorks Inc., Natick, MA), on a Pentium IV personal computer, 3.06 Ghz, 480 Mb random access memory (RAM). The time needed for the analysis of one image varied from a few seconds to a few minutes, depending on the data size. The required operator interaction consists of one point selection in the image, then the analysis is completely automatic. Therefore, our method is less user demanding than manual segmentation.

In our numerical experiments, we have used, for simplicity, $\Delta x = \Delta y = 1$ and $\Delta t = 0.1$, that is the classic configuration parameters used in [15]. Only the length parameter μ, which has a scaling role, is not the same in all experiments. If we have to detect many objects and of any size, μ should be small. If we have to detect only larger objects, and to not detect smaller objects (like points, due to the noise), then μ has to be larger. We will give the exact value of μ each time, together with the initial level set function ϕ_0. In Fig. 5 we present the result of the segmentation with different values of the parameter μ to explain its role. In order to find the relationship between μ and the curvature, we consider some circles of different radius (the radius of the circle is the inverse of curvature). The first has a radius of 0.5 pixels, and the last of 6 pixels (the step is of 0.5 pixels). The initial condition for this test was a multiple distance function automatically generated and independent from the image:

$$\phi_{md}(x, y) = \sum_i \sum_j \phi_0(x_0 + i\Delta x,\, y_0 + j\Delta y). \quad (15)$$

The test required 500 iterations before the flow reached the steady state. If $\mu = 0.001$ then all the objects are correctly detected, increasing μ it is possible to segment

TABLE I
EXPERIMENTAL DETAILS OF THE IMAGES WE USED IN THE STUDY.[1]

Data	Transducer	TCF[1] (MHz)	Acquisition[1]	Analysis[1]
1 fetal echography (Fig. 10)	Phased Array	5	transth	qual
1 right atrium (Fig. 7)	Phased Array	3.5	transth	qual
1 left atrium (Fig. 8)	Phased Array	3.5	transth	qual
11 left ventricles (Fig. 13 (up), 4)	Matrix	2.5	transth	quant
2 left ventricles (Fig. 9, 13 (down))	Phased Array	3.5	transth	quant
2 left ventricles (Fig. 12)	Phased Array	5	transes	quant

[1]TCF, Transducer center frequency; transth, transthoracic acquisition; transes, transesophageal acquisition; quant, quantitative analysis; qual, qualitative analysis.

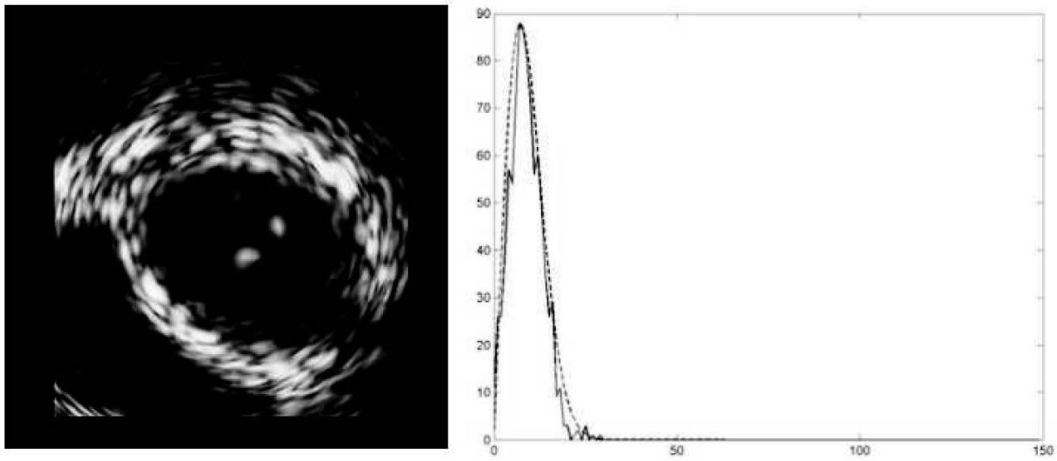

Fig. 4. On the right panel, example of the fitting between the Rayleigh probability density function and the measured histogram of a myocardial region of the B-scan image shown on the left.

only bigger objects. The relationship between μ and the radius is monotonic and can be represented easily in a logarithmic form (Fig. 6).

In the following images the observed pixels are modeled as Rayleigh distributed random variables with means depending on their position relative to the contours. We consider as an initial function a distance function:

$$\phi_d(x, y) = \sqrt{(x - x_0)^2 + (y - y_0)^2} + R,$$

where (x_0, y_0) is a reference point chosen anywhere within the object to be detected, and R is a constant term. The function $\phi_0(x, y) = \phi_d(x, y)$ has to be introduced as the initial condition of the flow.

In Figs. 7 and 8, we show anatomical structures segmentation from an echocardiographic image. To segment the right atrium chamber and the left atrium chamber, we choose a point internal to the chamber to be segmented (Figs. 7 and 8, upper left). We present some evolution steps to explain how our method works and observe that, due to the level set implementation, automatical change of topology is allowed. It is necessary that μ assumes a big value in order to conserve the stability of the solution: in this case $\mu = 2$. At the end of the evolution, the front coincides with the boundary of the chamber (Fig. 7 and Fig. 8, bottom right).

In Fig. 9 we consider a typical echocardiographic four chamber view acquisition. We want to segment the left ventricular chamber. The initial curve does not necessarily surround the object. This computation is performed with $\mu = 1$.

In the next images we consider a different initial function: a multiple distance function as for Fig. 5. In this case, we segment all the objects in the image. An example of the use of such function is shown in Fig. 10, in which we apply the segmentation method to a fetal echography. The parameter μ must be big because we are interested to segment a larger area ($\mu = 0.1$). By considering a multiple distance function as initial function, all the objects present in the image are segmented. In this case, both uterus and fetus have been detected. This can be an advantage (as in Fig. 5) or not, depending on the segmentation task.

B. Validation Results

To determine the reliability of the automated measurements versus the gold standard, represented by manual tracings, a set of 15 ultrasound images acquired with different echographic systems, was analyzed by an expert observer. The operator manually traced the contour of the anatomical structure of interest, obtaining the corresponding areas. Linear regression and Bland-Altman analyses

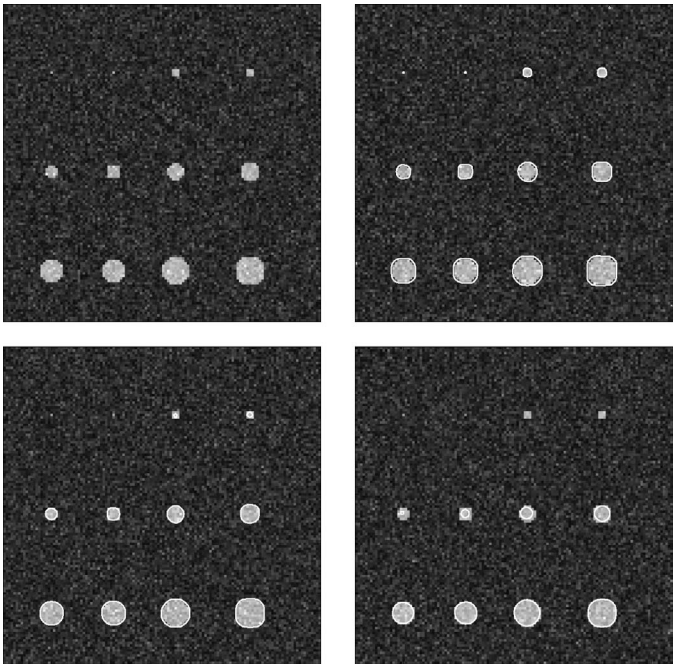

Fig. 5. Graphical representation of the calibration of μ: original figure (upper left); segmentation with $\mu = 0.001$ (upper right); segmentation with $\mu = 0.1$ (bottom left) and segmentation with $\mu = 2$ (bottom right). As shown in the four panels, for a small value of μ, small objects can be detected in the image; for greater values of μ, bigger objects can be evaluated better.

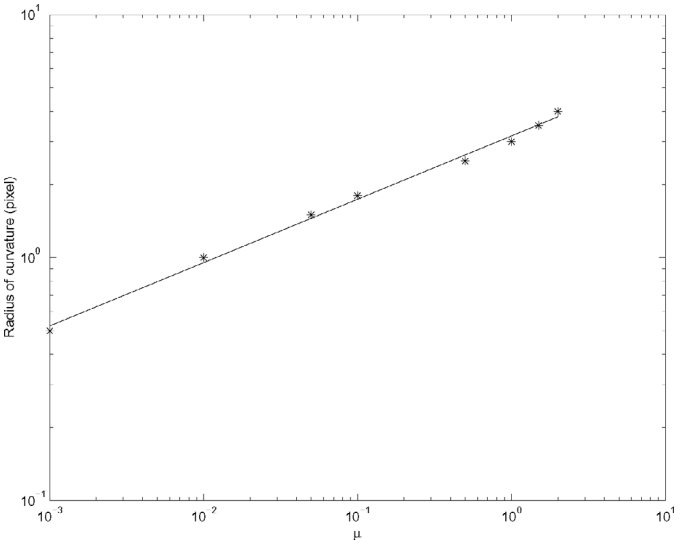

Fig. 6. Loglog graph of the relation between μ and the radius. The stars are the points obtained with the simulation; the straight line fits these points.

were performed between the manually traced areas, considered as the gold standard, and the measurements obtained applying our method. Moreover, the digitized manual contours also were overimposed and compared point-to-point to the corresponding level set contours by the computation of the Hausdorff distance [35], [36]: it measures the degree of mismatch between two sets of points, C_1 and C_2, by evaluating the distance between the point a of C_1 that is farthest from any point b of C_2 and vice versa:

$$H(C_1, C_2) = \max(h(C_1, C_2),\, h(C_2, C_1)), \qquad (16)$$

with $h(C_1, C_2) = \max_{a \in C_1} \min_{b \in C_2} \|a - b\|$.

The comparison between the automated versus the manually traced contours resulted in a very good agreement in the areas calculated with both techniques, with an excellent correlation ($r = 1$), and an absolute mean error, expressed in percentage of the gold standard value, of $2.7\% \pm 2.4\%$. Bland-Altman analysis resulted in a negligible negative bias of -0.17 cm^2 for the automated versus the manual measures, with the 95% confidence equal to 0.82 cm^2. In Fig. 11 the linear regression and Bland-Altman results are graphically reported. An example of the automated versus the manually traced contours is shown in Fig. 12 where the good correspondence can be appreciated. This was confirmed by the global results relevant to the Hausdorff distance in which a mean value of 1.1 pixel (range: $0.4 \div 1.9$ pixels) and a mean maximum value of 4.3 pixels (range: $2 \div 8$ pixels) were found versus the gold standard. The results of the analysis are summarized in Table II.

On five images we compared our maximum likelihood segmentation method with the original Chan and Vese formulation. We overimposed the contour obtained applying the methodology proposed by Chan and Vese [23] with the manual tracing. Minimizing the difference between the two contours we derived the best parameters' values for the Chan and Vese equation. Then we compared the contour obtained applying this choice for the parameters' values and the result of the maximum likelihood segmentation method. The two methodologies resulted in quite similar results: in particular the Hausdorff distance resulted in a mean value of 1.8 pixel (range: $1.2 \div 2.3$ pixels) and in a mean maximum value of 7.8 pixels (range: $5 \div 10$ pixels) versus the gold standard. The area values compared to manually traced areas resulted in a mean percentage error of -1.7% (range: $-14.5 \div 2.6\%$). Directly comparing the two methods with the gold standard on the same group of images, our method showed an absolute mean percentage error of 1.6% versus 4.2%, an improvement of the accuracy of a factor 2.7. This is relevant for quantitative evaluation of functionality parameters of the heart in clinical practice. The results of the analysis are summarized in Table III. Two examples are shown in Fig. 13. For the upper panel we found an error of 2.6% versus the manually traced contour's area and 0.1% versus the area calculated applying the maximum likelihood segmentation method. The maximum error and mean error for the Hausdorff distance were 8 pixels and 2.3 pixels, respectively, compared to the gold standard; the contour obtained with our method resulted in a maximum error and a mean error for the Hausdorff distance of 5 pixels and 1.5 pixels, respectively, compared to the gold standard. For the bottom panel, we found an error of -0.3% versus the manually traced contour's area and 0.2% versus the area calculated applying the maximum likelihood segmentation method. The maximum error and mean error for the Hausdorff distance were 8 pixels

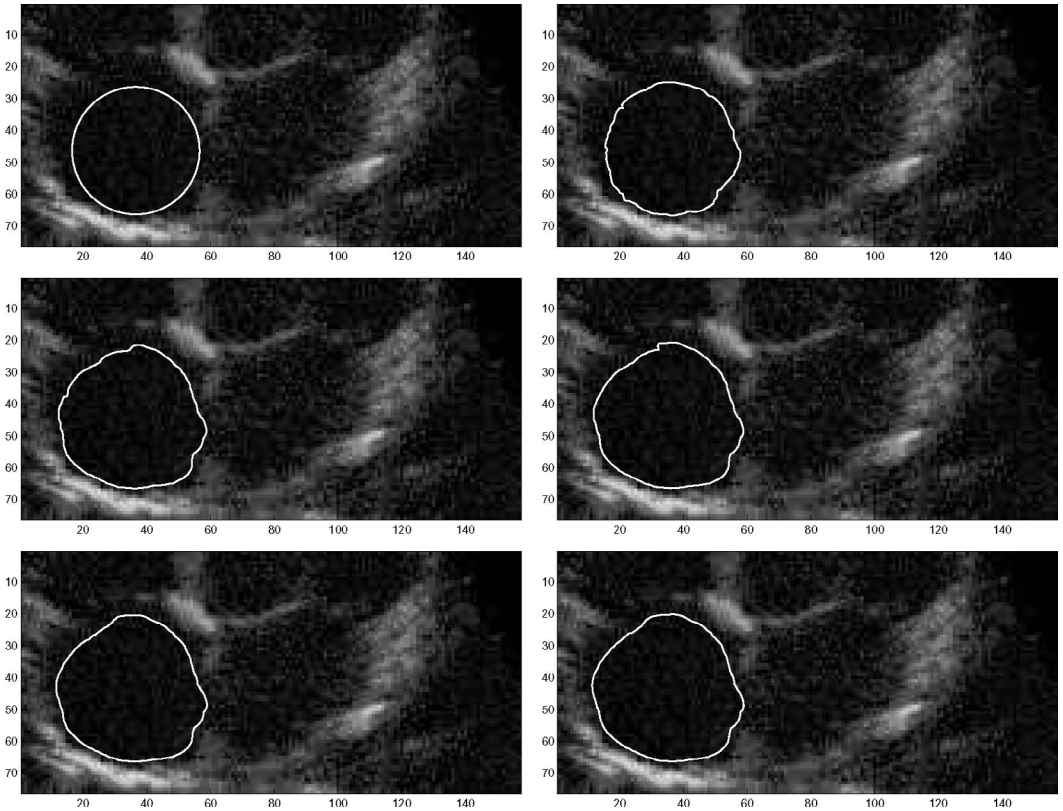

Fig. 7. Initial condition (upper left) and some evolution steps of the segmentation of a cardiac chamber from an echocardiographic acquisition. The final contour (bottom right) well represents the chamber boundary, even in the presented case of the right atrium. The convergence was reached in 200 iterations.

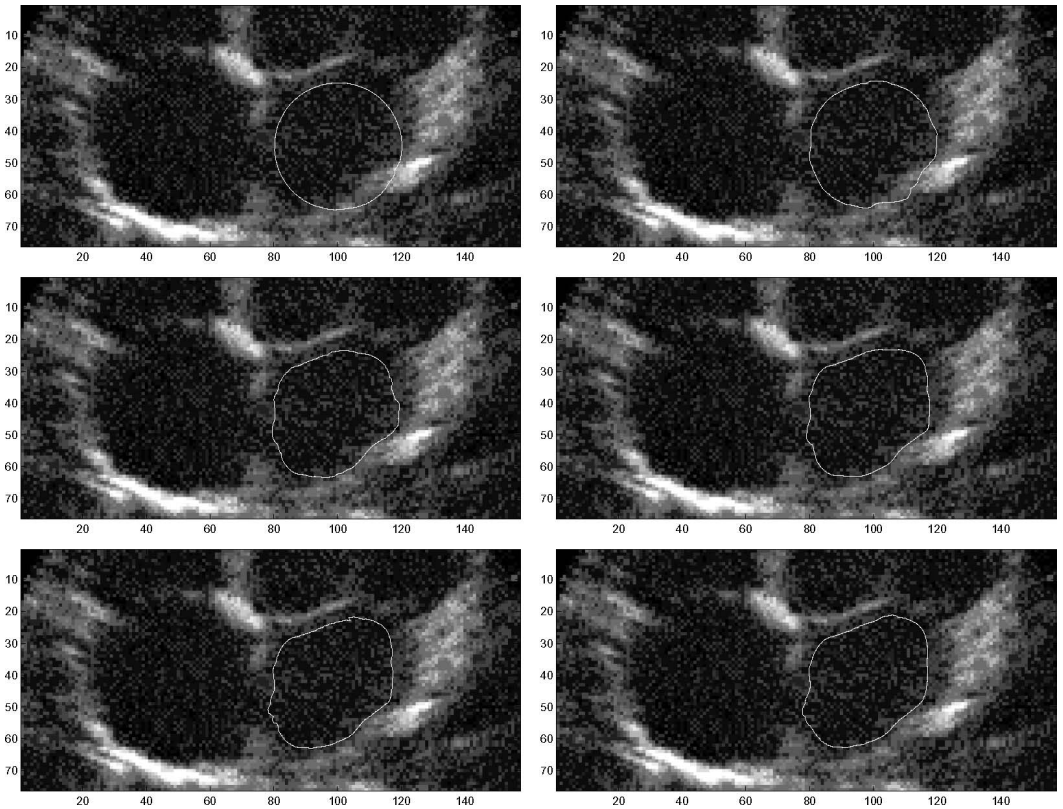

Fig. 8. Segmentation of anatomical structure from an echocardiographic image: initial condition (upper left) and final detected contour (bottom right) of the left atrium. The convergence was reached in 200 iterations.

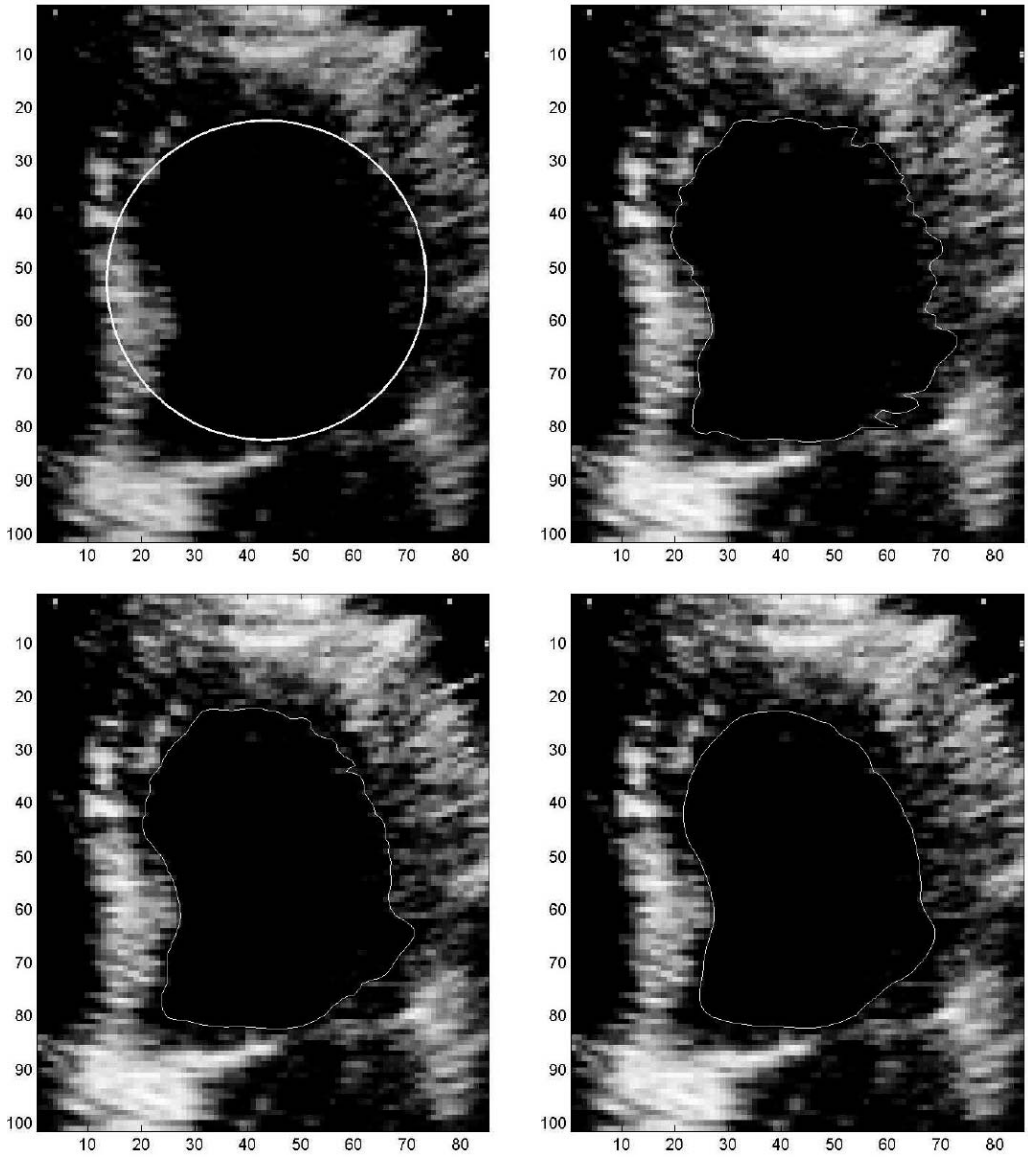

Fig. 9. Initial condition (upper left) and some evolution steps of the segmentation of left ventricle from a typical echocardiographic four chamber view acquisition. The convergence was reached in 150 iterations.

and 2.30 pixels, respectively, compared to the gold standard; the contour obtained with our method resulted in a maximum error and a mean error for the Hausdorff distance of 7 pixels and 1.9 pixels, respectively, compared to the gold standard.

V. Conclusions

A mathematical model and computational algorithm to segment ultrasound images has been presented. The technique is based on level-set methods and exploits the a priori knowledge about the statistical distribution of image gray levels. Because ultrasound images show a low signal/noise ratio, it is often dangerous to compute differential quantities of the image signal. The method we propose is good because it uses only integral quantities of the image and it does not introduce high-frequency noise. Only one parameter has to be set, and it allows one to choose easily the maximum curvature admissible in the segmentation. The initial condition can be either selected by the user as a distance function or automatically set as a multiple distance function. In the first case, used together with reinitialization, the flow stops when a local minimum close to the initial condition is reached. In the latter one, the segmentation of all the objects in the image is reached, as in [23].

Appendix A
PDF Optimal Parameters Estimation

In this section we present how to estimate the optimal parameters of the pdf with a maximum likelihood approach, accordingly with [25]. The Rayleigh probability function is defined by:

$$p(I(x,y)) = \frac{I(x,y)}{\sigma^2} \exp\left(-\frac{I(x,y)^2}{2\sigma^2}\right),$$

where σ is the parameter of the law and $I(x,y)$ take discrete values. Let σ_i and σ_e be the parameter values for the target and for the background pixels. The log-likelihood is thus:

$$l(I,C,\sigma_i,\sigma_e) = \log\left(\prod_{(x,y)\in\Omega} p(I(x,y))\right) =$$
$$\sum_{(x,y)\in\Omega_i} \left(\log(I(x,y)) - I^2(x,y)/(2\sigma_i^2) - 2\log(\sigma_i)\right) +$$
$$\sum_{(x,y)\in\Omega_e} \left(\log(I(x,y)) - I^2(x,y)/(2\sigma_e^2) - 2\log(\sigma_e)\right) =$$
$$\sum_{(x,y)\in\Omega_i} \log(I(x,y)) - \sum_{(x,y)\in\Omega_i} I^2(x,y)/(2\sigma_i^2) -$$
$$2A_i\log(\sigma_i) + \sum_{(x,y)\in\Omega_e} \log(I(x,y)) -$$
$$\sum_{(x,y)\in\Omega_e} I^2(x,y)/(2\sigma_e^2) = 2A_e\log(\sigma_e),$$

where A_i and A_e are, respectively, the number of pixels of the target and of the background. The maximum likelihood estimate of the parameters σ_i and σ_e are the values that maximize $l(I,C,\sigma_i,\sigma_e)$ and are obtained by equating to zero the first derivative with respect to σ_i:

$$\partial l/\partial\sigma_i = 2\sum_{(x,y)\in\Omega_i} I^2(x,y)/(2\sigma_i^3) - 2A_i/\sigma_i = 0,$$

and to σ_e:

$$\partial l/\partial\sigma_e = 2\sum_{(x,y)\in\Omega_e} I^2(x,y)/(2\sigma_e^3) - 2A_i/\sigma_e = 0.$$

Then the optimal values for the parameters can be computed easily:

$$\hat{\sigma}_i^2 = \sum_{(x,y)\in\Omega_i} I^2(x,y)/(2A_i),$$

and:

$$\hat{\sigma}_e^2 = \sum_{(x,y)\in\Omega_e} I^2(x,y)/(2A_e).$$

By introducing these estimates back in the log-likelihood, we obtain:

$$l(I,C,\hat{\sigma}_i,\hat{\sigma}_e) = \sum_{(x,y)\in\Omega} \log I(x,y) - N$$
$$- A_i\log\left(\sum_{(x,y)\in\Omega_i} I^2(x,y)/(2A_i)\right)$$
$$- A_e\log\left(\sum_{(x,y)\in\Omega_e} I^2(x,y)/(2A_e)\right),$$

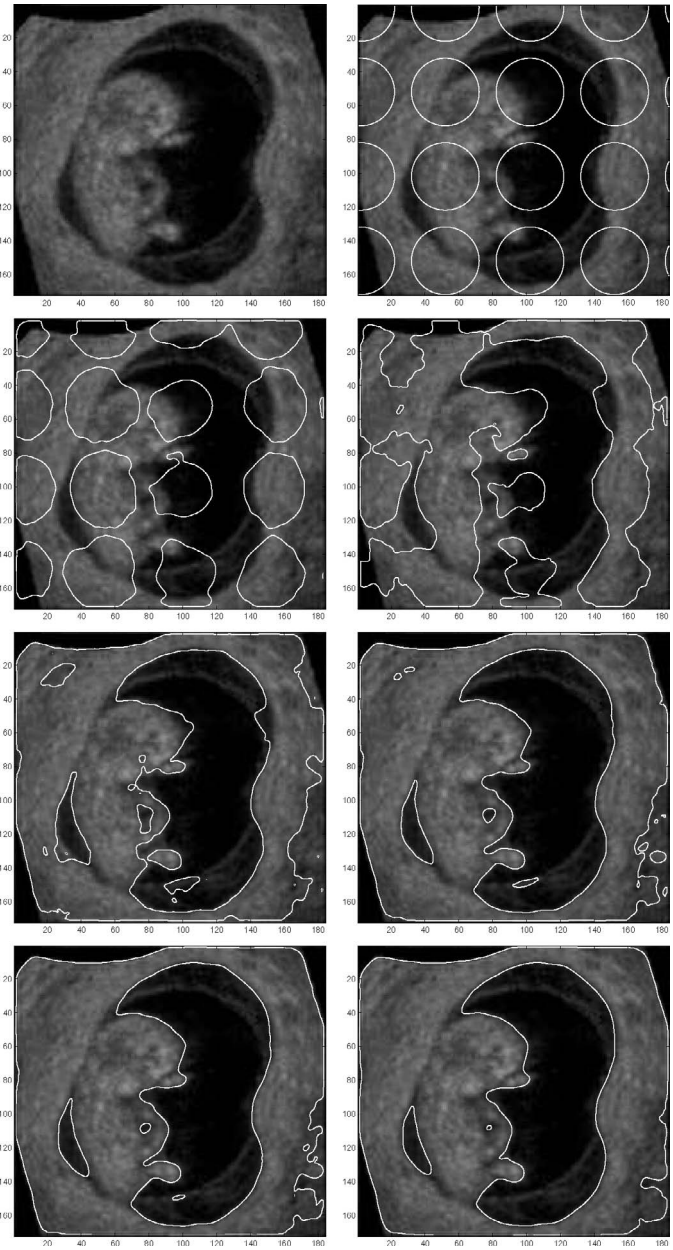

Fig. 10. Segmentation of fetal echogram: the original image (upper left), the distance function (upper right), some steps of the curve evolution, and the segmented boundary (bottom right). The convergence was reached in 300 iterations.

where N is the total number of pixels. All the terms of the right-hand side not depending on the partition Ωi and Ωe can be omitted. Then we find the criterion used in (5):

$$J(I,C) = -l(I,C,\hat{\sigma}_i,\hat{\sigma}_e) =$$
$$A_i\log\left(\sum_{(x,y)\in\Omega_i} I^2(x,y)/A_i\right) +$$
$$A_e\log\left(\sum_{(x,y)\in\Omega_e} I^2(x,y)/A_e\right),$$

in agreement with [25].

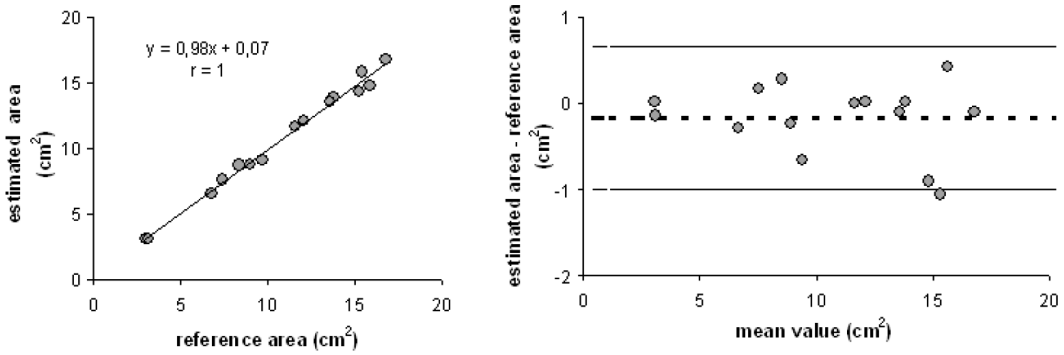

Fig. 11. Linear regression analysis (left panel) and Bland-Altman analysis (right panel) comparing manual tracing estimates and area values obtained applying our maximum likelihood segmentation method.

TABLE II
STATISTICAL ANALYSIS RESULTS COMPARING THE MAXIMUM LIKELIHOOD SEGMENTATION RESULTS WITH THE MANUAL TRACING RESULTS.

	Linear regression equation	r	bias ± S.D.	Hausdorff distance (pixel) mean distance mean of maximum distances
Max likelihood model	$y = 0.98x + 0.07$	1	$-0.17 + 0.41$	1.1 (range, 0.4 ± 1.9) 4.3 (range, 2 ± 8)

TABLE III
RESULTS OF THE COMPARISON BETWEEN THE RESULTS OBTAINED WITH THE MAXIMUM LIKELIHOOD SEGMENTATION MODEL AND THE CHAN VESE MODEL.

	Maximum likelihood segmentation	Chan-Vese model
Abs mean error vs. reference (mean ± SD, %)	1.6 ± 1.8	4.2 ± 5.8
Hausdorff distance (pixel)		
mean distance	1.3 (range, 0.9 ± 1.9)	1.8 (range, 1.2 ± 2.3)
mean of maximum distances	4.4 (range, 2 ± 7)	7.8 (range, 5 ± 10)

APPENDIX B
FUNCTIONAL MINIMIZATION

In this section we explain how to minimize the functional (7). We will derive the Euler-Lagrange equations and the associated flow.

The problem can be expressed using the first variation of the functional with respect to ϕ. Introducing a test function ψ of the same type of ϕ, it is necessary to solve the following equation:

$$\lim_{t\to 0} \frac{1}{t}(F(\phi + t\psi) - F(\phi)) = 0.$$

In order to compute this variation, we consider a slightly regularized version of the Heaviside function H, and of the one-dimensional Dirac measure δ, denoted, respectively, by H_ε and δ_ε, as follows:

$$H_\varepsilon(x) = \frac{1}{2}\left(1 + \frac{2}{\pi}\arctan\left(\frac{x}{\varepsilon}\right)\right),$$
$$\delta_\varepsilon(x) = \frac{d}{dx}H_\varepsilon(x) = \frac{1}{\pi}\cdot\frac{\varepsilon}{\varepsilon^2 + x^2}.$$

Thus the minimization problem is so expressed:

$$\begin{aligned}
&\lim_{t\to 0}\frac{1}{t}(F(\phi + t\psi) - F(\phi)) \\
&= \int_\Omega \mu\left(\delta'_\varepsilon(\phi)|\nabla\phi|\psi + \delta_\varepsilon(\phi)\frac{\nabla\phi\nabla\psi}{|\nabla\psi|}\right)dxdy \\
&- \int_\Omega \delta_\varepsilon(\phi)\left[\log\left(\frac{1}{\int_\Omega H_\varepsilon(\phi)dxdy}\int_\Omega I^2 H_\varepsilon(\phi)dxdy\right)\right. \\
&+ \frac{I^2\int_\Omega H_\varepsilon(\phi)dxdy - \int_\Omega I^2 H_\varepsilon(\phi)dxdy}{\int_\Omega I^2 H_\varepsilon(\phi)dxdy} \\
&- \log\left(\frac{1}{\int_\Omega(1 - H_\varepsilon(\phi))dxdy}\int_\Omega I^2(1 - H_\varepsilon(\phi))dxdy\right) \\
&\left.- \frac{I^2\int_\Omega(1-H_\varepsilon(\phi))dxdy - \int_\Omega I^2(1-H_\varepsilon(\phi))dxdy}{\int_\Omega I^2(1-H_\varepsilon(\phi))dxdy}\right]\psi dxdy = 0.
\end{aligned}$$

Integrating by parts and using Green's theorem, we obtain:

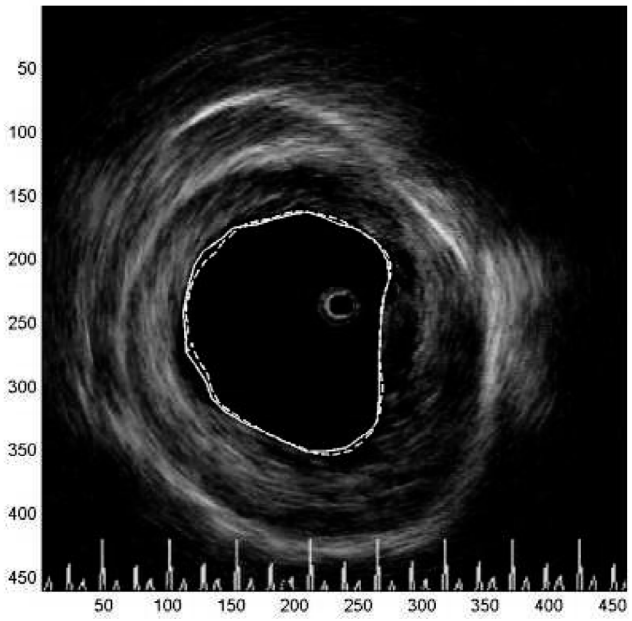

Fig. 12. Example of the extracted contour obtained by the maximum likelihood segmentation method (white dashed line) compared to the manual tracing contour (white solid line) both applied to a cross sectional intracardiac acquisition with a catheter inserted through a sheath.

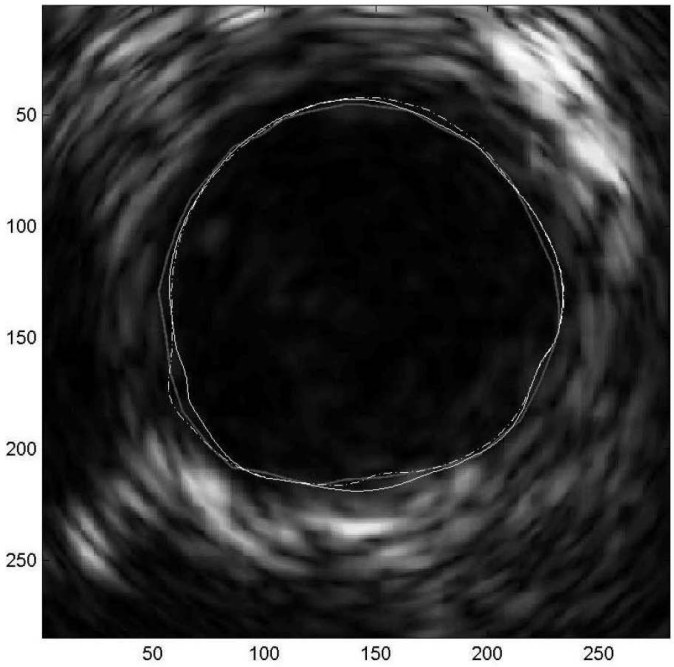

$$\int_\Omega \mu\delta'_\varepsilon(\phi)|\nabla\phi|\psi dxdy + \int_{\partial\Omega} \mu\frac{\delta_\varepsilon(\phi)}{|\nabla\phi|}\frac{\partial\phi}{\partial n}\psi ds - \int_\Omega \mu\nabla\left(\delta_\varepsilon(\phi)\frac{\nabla\phi}{|\nabla\phi|}\right)\psi dxdy - \int_\Omega \delta_\varepsilon(\phi)\left[\log\left(\frac{1}{\int_\Omega H_\varepsilon(\phi)dxdy}\int_\Omega I^2 H_\varepsilon(\phi)dxdy\right) + \frac{I^2\int_\Omega H_\varepsilon(\phi)dxdy - \int_\Omega I^2 H_\varepsilon(\phi)dxdy}{\int_\Omega I^2 H_\varepsilon(\phi)dxdy} - \log\left(\frac{1}{\int_\Omega(1-H_\varepsilon(\phi))dxdy}\int_\Omega I^2(1-H_\varepsilon(\phi))dxdy\right) - \frac{I^2\int_\Omega(1-H_\varepsilon(\phi))dxdy - \int_\Omega I^2(1-H(\phi))dxdy}{\int_\Omega I^2(1-H_\varepsilon(\phi))dxdy}\right]\psi dxdy = 0.$$

Formally developing the divergence operator, we finally obtain:

$$-\int_\Omega \mu\delta_\varepsilon(\phi)\nabla\left(\frac{\nabla\phi}{|\nabla\phi|}\right)\psi dxdy + \int_{\partial\Omega}\mu\frac{\delta_\varepsilon(\phi)}{|\nabla\phi|}\frac{\partial\phi}{\partial n}\psi ds - \int_\Omega \delta_\varepsilon(\phi)\left[\log\left(\frac{1}{\int_\Omega H_\varepsilon(\phi)dxdy}\int_\Omega I^2 H_\varepsilon(\phi)dxdy\right) + \frac{I^2\int_\Omega H_\varepsilon(\phi)dxdy - \int_\Omega I^2 H_\varepsilon(\phi)dxdy}{\int_\Omega I^2 H_\varepsilon(\phi dxdy)} - \log\left(\frac{1}{\int_\Omega(1-H_\varepsilon(\phi))dxdy}\int_\Omega I^2(1-H_\varepsilon(\phi))dxdy\right) - \frac{I^2\int_\Omega(1-H_\varepsilon(\phi))dxdy - \int_\Omega I^2(1-H_\varepsilon(\phi))dxdy}{\int_\Omega I^2(1-H_\varepsilon(\phi))dxdy}\right]\psi dxdy = 0.$$

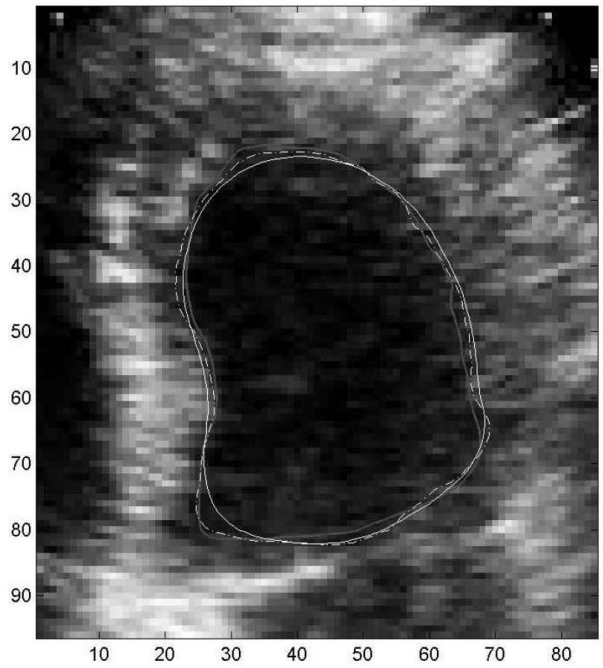

Fig. 13. Two examples of the extracted contour obtained by the Chan Vese original method (white solid line) and the maximum likelihood segmentation method (white dashed line) compared to the manual tracing contour (gray line).

This expression must vanish for all test function ψ. Thus we obtain:

$$
\begin{aligned}
0 = \delta_\varepsilon(\phi))\Bigg[& \mu div\left(\frac{\nabla\phi}{|\nabla\phi|}\right) \\
& + \log\left(\frac{1}{\int_\Omega H_\varepsilon(\phi)dxdy}\int_\Omega I^2 H_\varepsilon(\phi)dxdy\right) \\
& + \frac{I^2\int_\Omega H_\varepsilon(\phi)dxdy - \int_\Omega I^2 H_\varepsilon(\phi)dxdy}{\int_\Omega I^2 H_\varepsilon(\phi)dxdy} \\
& - \log\left(\frac{1}{\int_\Omega (1-H_\varepsilon(\phi))\,dxdy}\int_\Omega I^2\,(1-H_\varepsilon(\phi)dxdy)\right) \\
& - \frac{I^2\int_\Omega (1-H_\varepsilon(\phi))dxdy - \int_\Omega I^2(1-H_\varepsilon(\phi))dxdy}{\int_\Omega I^2(1-H_\varepsilon(\phi))dxdy}\Bigg].
\end{aligned}
$$

If $\varepsilon \to 0$, the approximation $H_\varepsilon\, e\, \delta_\varepsilon$ converge to H and δ, and we finally obtain the Euler-Lagrange (8). From this equation it is easy to determine the associated flow (9).

References

[1] L. Herlin, D. Bereziat, G. Giraudon, C. Nguyen, and C. Graffigne, "Comparison of different Markov random fields model for segmenting echocardiographic images," Research report, INRIA, 1994.

[2] L. Herlin, D. Bereziat, G. Giraudon, C. Nguyen, and C. Graffigne, "Segmentation of echocardiographic images with Markov fields," in *Proc. Eur. Conf. Comput. Vision*, 1994, pp. 201–206.

[3] E. A. Ashton and K. J. Parkers, "Multiple resolution Bayesian segmentation of ultrasound images," *Ultrason. Imag.*, vol. 17, pp. 291–304, 1999.

[4] X. Papademetris, A. J. Sinusas, D. P. Dione, and J. S. Duncan, "Estimation of 3D left ventricular deformation from echocardiography," *Med. Image Analysis*, vol. 5, pp. 17–28, 2001.

[5] D. Boukerroui, A. Baskurt, J. A. Noble, and O. Basset, "Segmentation of ultrasound images-multiresolution 2D and 3D algorithm based on global and local statistics," *Pattern Recognition Lett.*, vol. 24, pp. 779–790, 2003.

[6] M. Mulet-Parada and J. A. Noble, "2D+T acoustic boundary detection in echocardiography," *Med. Image Analysis*, vol. 4, pp. 21–30, 2000.

[7] E. D. Angelini, A. F. Laine, S. Takuma, J. W. Holmes, and S. Homma, "LV volume quantification via spatiotemporal analysis of real-time 3-D echocardiography," *IEEE Trans. Med. Imag.*, no. 6, pp. 457–469, 2001.

[8] J. Feng, W. Lin, and C. Chen, "Epicardial boundary detection using fuzzy reasoning," *IEEE Trans. Med. Imag.*, vol. 10, pp. 187–199, 1991.

[9] S. K. Satarehdan and J. J. Soraghan, "Automatic cardiac LV boundary detection and tracking using hybrid fuzzy temporal and fuzzy multiscale edge detection," *IEEE Trans. Biomed. Eng.*, vol. 46, pp. 1364–1378, 1999.

[10] G. I. Sanchez-Ortiz, G. J. T. Wright, N. Clarke, J. Declerck, A. Banning, and J. A. Noble, "Automated 3D echocardiography analysis compared with manual delineation and MUGA," *IEEE Trans. Med. Imag.*, vol. 21, no. 9, pp. 1069–1076, 2002.

[11] C. Kotropoulos, X. Magnisalis, I. Pitas, and M. G. Strintzis, "Nonlinear ultrasonic image processing based on signal-adaptive filters and self-organizing neural networks," *IEEE Trans. Image Processing*, vol. 3, pp. 65–77, 1994.

[12] G. Coppini, R. Poli, and R. Valli, "Recovery of 3-D shape of the left ventricle from echocardiographic images," *IEEE Trans. Med. Imag.*, vol. 14, pp. 301–317, 1995.

[13] M. Kass, A. Witkin, and D. Terzopoulos, "Snakes: Active contour models," *Int. J. Comput. Vision*, vol. 1, pp. 321–331, 1988.

[14] R. Malladi, J. A. Sethian, and B C. Vemuri, "Shape modeling with front propagation: A level set approach," *IEEE Trans. Pattern Anal. Machine Intell.*, vol. 17, pp. 158–175, 1995.

[15] S. Osher and J. A. Sethian, "Front propagating with curvature dependent speed: Algorithms based on Hamilton Jacobi formulation," *J. Comput. Phys.*, vol. 79, pp. 12–49, 1988.

[16] A. Sarti and R. Malladi, "A Geometric Level Set Model for Ultrasound Image Analysis," in *Computing Sciences Directorate Mathematics Department*. University of California, Berkeley, CA, 1999.

[17] N. Lin, W. Yu, and J. S. Duncan, "Combinative multi-scale level set framework for echocardiographic image segmentation," *Med. Image Analysis*, vol. 7, no. 4, pp. 529–537, 2003.

[18] N. Paragios, "A level set approach for shape-driven segmentation and tracking of the left ventricle," *IEEE Trans. Med. Imag.*, vol. 22, no. 6, pp. 773–776, 2003.

[19] Y. Chen, F. Huang, H. D. Tagare, R. Murali, D. Wilson, and E. A. Geiser, "Using prior shape and intensity profile in medical image segmentation," *ICCV*, pp. 1117–1124, 2003.

[20] A. Sarti, R. Malladi, and J. A. Sethian, "Subjective surfaces: A method for completion of missing boundaries," *PNAS*, vol. 12, no. 97, pp. 6258–6263, 2000.

[21] C. Corsi, M. Borsari, A. Sarti, C. Lamberti, A. Travaglini, T. Shiota, and J. D. Thomas, "Left ventricular endocardial surface detection based on real time 3D echocardiographic data," *Eur. J. Ultrasound*, vol. 13, pp. 41–51, 2001.

[22] C. Corsi, G. Saracino, A. Sarti, and C. Lamberti, "Left ventricular volume estimation for real-time-dimensional echocardiography," *IEEE Trans. Med. Imag., Special Issue on New Trends on Cardiovascular Image Analysis*, vol. 21, pp. 1202–1208, 2002.

[23] T. F. Chan and L. A. Vese, "Active contours without edges," *IEEE Trans. Image Processing*, vol. 10, no. 2, pp. 266–277, 2001.

[24] A. C. Bovik, "On detecting edges in speckle imagery," *IEEE Trans. Acoust. Speech Signal Processing*, vol. 36, no. 10, pp. 1618–1627, 1988.

[25] C. Chesnaud, P. Refregier, and V. Boulet, "Statistical region snake-based segmentation adapted to different physical noise models," *IEEE Trans. Pattern Anal. Machine Intell.*, vol. 21, no. 11, pp. 1145–1157, 1999.

[26] A. Azzalini, *Statistical Inference-Based on the Likelihood*. New York: Chapman and Hall, 1996.

[27] Y. C. Chang, T. Y. Hou, B. Merriman, and S. Osher, "A level set formulation of Eulerian interface capturing methods for incompressible fluid flows," *J. Computat. Phys.*, vol. 124, pp. 449–464, 1996.

[28] H. Zhao, T. F. Chan, B. Merriman, and S. Osher, "A variational level set approach to multiphase motion," *J. Computat. Phys.*, vol. 127, pp. 179–195, 1996.

[29] J. A. Sethian, *Level Set Methods: Evolving Interface in Geometry, Fluid Mechanics, Computer Vision, and Materials Science*. Cambridge Univ. Press, 1996.

[30] M. Sussman, P. Smereka, and S. Osher, "A level set approach for computing solutions to incompressible two-phase flow," *J. Computat. Phys.*, vol. 119, pp. 146–159, 1994.

[31] R. J. LeVeque, *Numerical Method for Conservation Laws*. Boston: Birkhauser, 1992.

[32] R. F. Wagner, S. W. Smith, J. M. Sandrik, and H. Lopez, "Statistics of speckle in ultrasound B-scans," *IEEE Trans. Sonics Ultrason.*, vol. 30, no. 3, pp. 156–163, 1983.

[33] C. B. Burckhardt, "Speckle in ultrasound B-mode scans," *IEEE Trans. Sonics Ultrason.*, vol. 25, no. 1, pp. 1–6, 1978.

[34] G. Georgiou and F. S. Cohen, "Statistical characterization of diffuse scattering in ultrasound images," *IEEE Trans. Ultrason., Ferroelect., Freq. Contr.*, vol. 45, no. 1, pp. 57–64, 1998.

[35] D. P. Huttenlocher, G. A. Klanderman, and W. J. Rucklidge, "Comparing images using the Hausdorff distance," *IEEE Trans. Pattern Anal. Machine Intell.*, vol. 15, no. 9, pp. 850–863, 1993.

[36] E. Belogay, C. Cabrelli, U. Molter, and R. Shonkwiler, "Calculating the Hausdorff distance between curves," *Information Processing Lett.*, vol. 64, pp. 17–22, 1997.

Alessandro Sarti was born in Modena, Italy, in 1964. He earned his Laurea Degree in electronic engineering from the University of Bologna, Bologna, Italy, in 1992 with a score of 100/100 cum laude. He received the Ph.D. degree in bioengineering from the University of Bologna in 1996. From 1997 to 2000 he was appointed with a Postdoc position at the Mathematics Department of the University of California, Berkeley, and the Mathematics Department of the Lawrence Berkeley National Laboratory in Berlekey, CA, working in the group of James Sethian and Alexander Chorin.

Since 2001 he has had a permanent position at the University of Bologna, where he teaches the classes of bioimaging. In 2003 he was also appointed as Maitre de Recherche at CREA, Ecole Polytechnique, Paris, France. He wrote more than 80 publications in the field of computer vision, medical imaging, and biologically based models of visual perception. With Giovanna Citti, he is the scientific responsible of the Gruppo Interdipartimentale di Visione, an interdisciplinary group comprehending the Dipartimento di Elettronica, Informatica e Sistemistica and the Dipartimento di Matematica of the Bologna University. In the last 3 years he gave lectures at the University of Yale, University of California at Los Angeles, University of California at Berkeley, Freie Universitat Berlin, Ecole Normale Superieure Cachan, Palazzone di Cortona Scuola Normale Superiore di Pisa.

Cristiana Corsi received her doctoral degree in electronic engineering from the University of Bologna, Bologna, Italy, in 1997 and her Ph.D. degree in bioengineering from the Department of Electronics, Computer Science and Systems at the University of Bologna in 2001. She spent six months visiting at the Mathematics Department of the University of California, Berkeley, and the Mathematics Department of the Lawrence Berkeley National Laboratory in Berkeley, working on level set methods applied to medical data processing.

Currently she holds a Postdoctoral Research grant at the University of Bologna. Her research interests include new expertized and advanced technologies and methods applied to medical data processing, in particular echocardiographic and magnetic resonance data.

Elena Mazzini was born in 1977. She received the B.Eng. degree in electronics and biomedical engineering from the University of Bologna, Bologna, Italy, in 2001.

From 2001 to 2002, she joined the university for research in the field of medical image segmentation. She is currently working for Medtronic Inc., Minneapolis, MN, in the area of cardiac rhythm disorders.

Claudio Lamberti received the doctoral degree in mechanical engineering from the University of Bologna, Bologna, Italy, in 1974. In 1978 he received the post-graduate degree in biomedical technology from the University of Bologna School of Medicine.

He is currently associate professor at the Department of Electronics, Computer Science and Systems of the University of Bologna. Since 1991 he has been in charge at the University of Bologna of the course Computer and Systems Science in Health Care. His research activity is focused on biomedical signal and image processing and biomedical technology assessment.

He has served on the Board of the Centro Ricerche e Studi Tecnologie Biomediche e Sanitarie (CRSTBS) at Scientific Park of Trieste, Italy, during 1989–1998. He also has served on the Board of the Associazione Italiana degli Ingegneri Clinici (AIIC) since 1993. He has published several papers on arrythmias recognition, left ventricular wall motion, echocardiography image processing, estimation of motion in 3-D echocardiography, computer aided virtual surgery, and computer systems for management of biomedical technology.